Acta Crystallographica Section D
Biological Crystallography
ISSN 0907-4449

'In crystallo' substrate binding triggers major domain movements and reveals magnesium as a co-activator of *Trypanosoma brucei* pyruvate kinase

Wenhe Zhong,[a]‡ Hugh P. Morgan,[a]‡ Iain W. McNae,[a] Paul A. M. Michels,[a,b] Linda A. Fothergill-Gilmore[a] and Malcolm D. Walkinshaw[a]*

[a]Centre for Translational and Chemical Biology, School of Biological Sciences, The University of Edinburgh, Mayfield Road, Edinburgh EH9 3JR, Scotland, and [b]Research Unit for Tropical Diseases, de Duve Institute and Laboratory of Biochemistry, Université catholique de Louvain, Avenue Hippocrate 74, B-1200 Brussels, Belgium

‡ These authors contributed equally to this work.

Correspondence e-mail: m.walkinshaw@ed.ac.uk

Received 7 February 2013
Accepted 20 May 2013

PDB References: *Tb*PYK–F26BP–Mg, 4hyw; *Tb*PYK–F26BP–PEP–Mg, 4hyv

The active site of pyruvate kinase (PYK) is located between the AC core of the enzyme and a mobile lid corresponding to domain B. Many PYK structures have already been determined, but the first 'effector-only' structure and the first with PEP (the true natural substrate) are now reported for the enzyme from *Trypanosoma brucei*. PEP soaked into crystals of the enzyme with bound allosteric activator fructose 2,6-bisphosphate (F26BP) and Mg^{2+} triggers a substantial 23° rotation of the B domain '*in crystallo*', resulting in a partially closed active site. The interplay of side chains with Mg^{2+} and PEP may explain the mechanism of the domain movement. Furthermore, it is apparent that when F26BP is present but PEP is absent Mg^{2+} occupies a position that is distinct from the two canonical Mg^{2+}-binding sites at the active site. This third site is adjacent to the active site and involves the same amino-acid side chains as in canonical site 1 but in altered orientations. Site 3 acts to sequester Mg^{2+} in a 'priming' position such that the enzyme is maintained in its R-state conformation. In this way, Mg^{2+} cooperates with F26BP to ensure that the enzyme is in a conformation that has a high affinity for the substrate.

1. Introduction

Glycolytic enzymes have been indicated as potential drug targets in trypanosomatid parasites such as *Trypanosoma brucei*, *T. cruzi* and *Leishmania* spp. (Verlinde *et al.*, 2001). Together, these parasites cause widespread debilitating diseases, primarily in tropical and subtropical parts of the world. Most of these diseases are fatal if untreated, but unfortunately many existing drugs have important undesirable side effects and resistance is an increasingly severe problem (Baker *et al.*, 2012). Among the glycolytic enzymes, pyruvate kinase (PYK) has been validated by RNAi experiments as a suitable drug target in *T. brucei* (Albert *et al.*, 2005).

PYK catalyses the last reaction in the glycolytic pathway to yield ATP and pyruvate from ADP and phospho*enol*pyruvate (PEP) and is typically a tetrameric enzyme, with each subunit made up of four domains (Fig. 1). The active site is located between the A and B domains, and is 40 Å distant from the effector site that is contained within the C domain. Adjacent C domains form the C–C or 'small' interface, as distinguished from the 'large' interface between adjacent A domains. The B domain has been observed in a variety of positions in different PYK crystal structures (Larsen *et al.*, 1997; Tulloch *et al.*, 2008; Morgan *et al.*, 2010) and forms a mobile lid over the active site. The A and C domains comprise the relatively static AC core of the enzyme (Fig. 1*b*). PYKs are generally well conserved and have retained similar sequences throughout evolution, with enzymes from even quite evolutionarily distant organisms

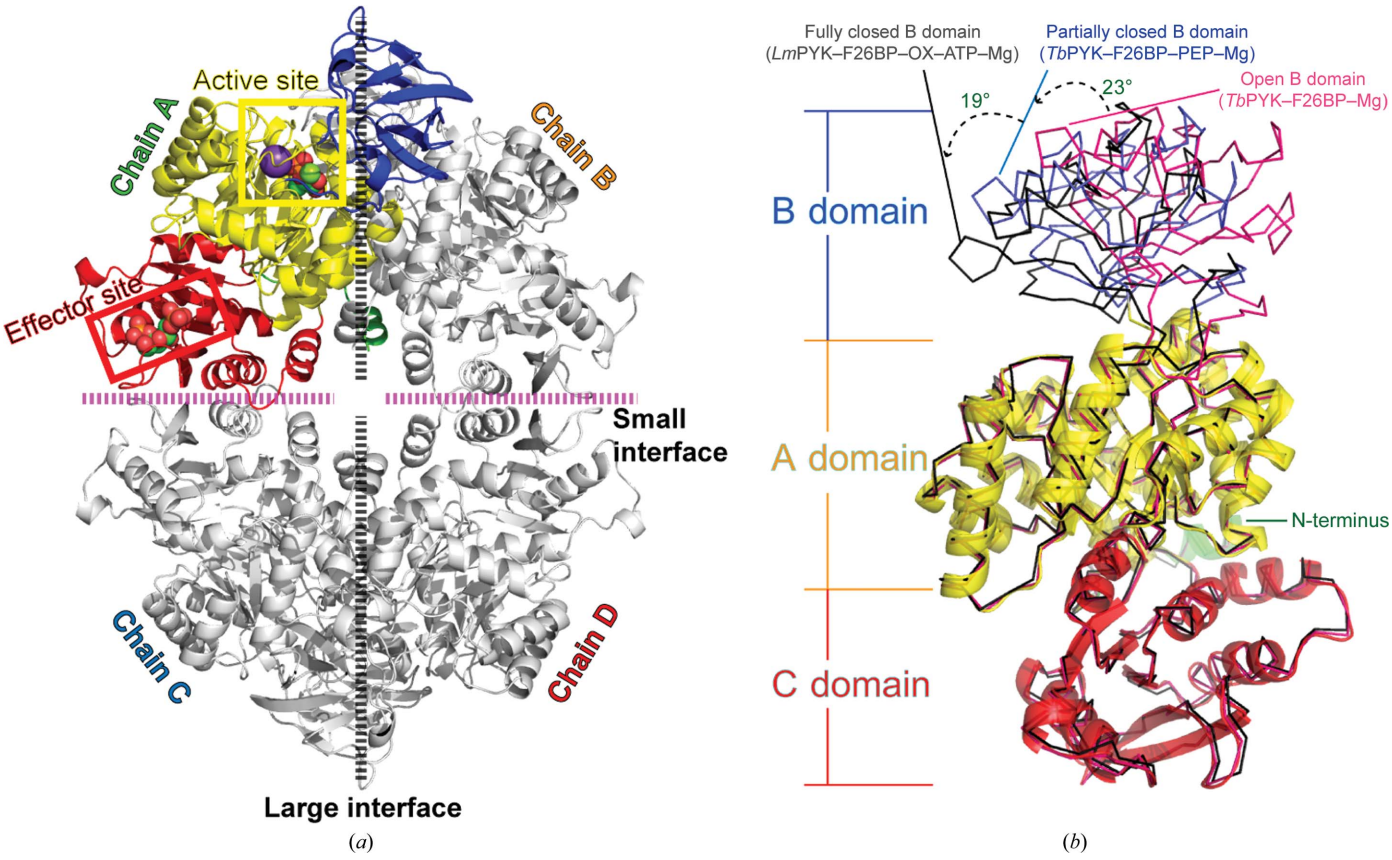

Figure 1
Tetrameric structure of PYK and the disposition of domains. (*a*) The four polypeptide chains of *Tb*PYK–F26BP–PEP–Mg. The large (A–A) and small (C–C) interfaces are indicated by dashed lines and the active and effector sites are boxed. Chain *A* shows the N-terminal domain (green; residues 2–18), A domain (yellow; residues 19–89 and 188–358), B domain (blue; residues 90–187) and C domain (red; residues 359–499). (*b*) An overlay of the AC domains from three PYK crystal structures: *Tb*PYK–F26BP–Mg (pink), *Tb*PYK–F26BP–PEP–Mg (blue) and *Lm*PYK–F26BP–OX–ATP–Mg (black; PDB entry 3hqp). The B-domain rotations of these PYK complexes were analysed using *DynDom* (Hayward *et al.*, 1997; Hayward & Berendsen, 1998). The B domain in *Tb*PYK–F26BP–Mg is in the open conformation, while the B domain in *Tb*PYK–F26BP–PEP–Mg is in the partially or half-closed conformation. *Lm*PYK–F26BP–OX–ATP–Mg has the B domain in its fully closed position.

showing 42–49% sequence identity (Supplementary Fig. S1 and Table S1[1]). The PYKs from trypanosomatids (*T. brucei*, *T. cruzi* and *Leishmania* spp.) are 74–81% identical in sequence.

PYKs are either constitutively active (as exemplified by the muscle isoenzyme M1 in mammals) or are allosterically activated and/or inhibited (essentially all other forms of PYK). Rabbit muscle M1PYK has been extensively studied (Larsen *et al.*, 1994, 1997; Wooll *et al.*, 2001; Williams *et al.*, 2006) and many mechanistic insights have been derived from structures of its complexes with various substrate analogues (PDB entries 1aqf, 1a49, 1a5u, 1f3w and 2g50). However, these structures provide little insight into the role of allosteric regulation by fructose bisphosphate (FBP) activators or of the cooperative binding of the substrate PEP, neither of which is observed in constitutively active PYKs. In particular, a structural understanding of the communication between the active site and the 40 Å distant effector site is incomplete. Here, we present a high-resolution structure of *T. brucei* PYK (*Tb*PYK) in complex with its allosteric activator fructose 2,6-bisphosphate (F26BP) and Mg^{2+}, which is the first 'effector-only' structure of an allosterically regulated PYK. This structure, together with the structure with added PEP, helps to provide a clear picture of the structural changes during the catalytic cycle of an allosterically regulated PYK.

More than 30 years have elapsed since the first purification protocol for PYK from bloodstream-form *Tb*PYK was reported (Flynn & Bowman, 1980). The enzyme was subsequently expressed in an *Escherichia coli* system and purified (Ernest *et al.*, 1998). However, determination of the crystal structure of *Tb*PYK has remained elusive, although the crystal structure of the corresponding enzyme from *L. mexicana* (*Lm*PYK; 74% sequence identity) has been extensively characterized (Rigden *et al.*, 1999; Morgan *et al.*, 2010). We now report modified protocols for the overexpression and purification of *Tb*PYK and its crystallization, which enabled the determination of its X-ray crystal structure in complex with the allosteric activator F26BP as well as Mg^{2+} and K^{+}. This crystal form was amenable to soaking with the physiological substrate PEP and yielded the first substrate-bound

[1] Supplementary material has been deposited in the IUCr electronic archive (Reference: CB5035). Services for accessing this material are described at the back of the journal.

structure of any PYK. Remarkably, the large domain movement induced by PEP binding can take place within the crystal lattice and shows conclusively that substrate binding alone can trigger closure of the B domain. Detailed comparison of the two crystal structures (*i.e.* with and without PEP) also revealed a possible regulatory role for Mg^{2+}.

2. Materials and methods

2.1. Materials

ADP, PEP, oxalate (OX), F16BP, F26BP, lactate dehydrogenase (LDH), polyethylene glycol (PEG) 8000, antibiotics and buffers were obtained from Sigma–Aldrich. NADH and EDTA-free protease-inhibitor mixture tablets were obtained from Roche, glycerol from BDH Prolabo, IPTG from Melford and salts from Fisher Scientific. Restriction enzymes and other enzymes used for cloning were purchased from New England BioLabs. Vector and *E. coli* competent cells were obtained from Novagen.

2.2. Cloning, overexpression and purification of untagged *Tb*PYK

*Tb*PYK (GenBank X57950.1) expressed in *E. coli* was insoluble using our original constructs even after expression-optimization trials. A series of gene codon-optimization procedures from GenScript were therefore applied to improve the efficiency of soluble expression in *E. coli*. The codon-optimized gene was synthesized and cloned into a pUC57 vector. In this construct, an *Nde*I restriction site and a *Bam*HI restriction site were present at the 5′ end and the 3′ end of the gene, respectively. The construct was then digested with the restriction endonucleases *Nde*I and *Bam*HI and the digested inserts were ligated into an *Nde*I–*Bam*HI-digested pET30a vector and verified by DNA sequencing after cloning. The verified construct (pET30a_*Tb*PYK) allows the expression of untagged *Tb*PYK.

Chemically competent *E. coli* BL21(DE3) cells were transformed with pET30a_*Tb*PYK and single colonies of transformed *E. coli* harbouring the optimized *Tb*PYK gene construct were picked from LB kanamycin (50 µg ml^{-1}) plates and used to inoculate 50 ml 2×TY medium containing 50 µg ml^{-1} kanamycin. Cultures were grown overnight at 310 K with agitation. 10 ml of overnight culture was used to inoculate 500 ml 2×TY medium containing 50 µg ml^{-1} kanamycin. The 500 ml cultures were grown to an OD_{600} of 0.6–0.8 and were incubated at 277 K for 30 min. Expression was induced by adding IPTG to a final concentration of 1 m*M*. Incubation was continued for 22 h at 291 K and the cells were harvested by centrifugation at 8000 rev min^{-1} in a JLA-9.1000 rotor for 15 min at 277 K. Cell pellets (3–3.5 g wet weight) from the 500 ml culture were then frozen in liquid nitrogen and stored at 193 K.

All enzyme purification was performed on ÄKTA (GE Healthcare) equipment at 279 K (Supplementary Fig. S2). Cell pellets from 500 ml *E. coli* cultures were thawed on ice and resuspended in 20 ml ice-cold cell-lysis buffer [50 m*M* triethanolamine–HCl (TEA) pH 7.9, 20 m*M* KCl, 10% glycerol] supplemented with EDTA-free protease inhibitors (Roche). Lysis was performed at 279 K by a single passage through a Constant System Cell Disruptor TS Series Benchtop instrument set to 152 MPa (equivalent to an instrument reading of 22 kpsi). Cellular debris was removed by centrifugation at 23 000 rev min^{-1} in a JA-25.50 rotor for 45 min at 279 K and the supernatant was filtered through a 0.22 µm syringe filter. The supernatant was then applied onto an ÄKTA system (100 ml min^{-1}, 10 MPa) fitted with two tandem ion-exchange columns (HiPrep DEAE FF 16/10 and HiPrep SP FF 16/10, fitted sequentially and pre-equilibrated in cell-lysis buffer). The columns were maintained at a constant flow rate of 2 ml min^{-1} throughout the whole purification process. Following loading of the clarified lysate, the columns were washed with three column volumes (CVs) of cell-lysis buffer. The flowthrough was collected in 10 ml fractions.

The target enzyme *Tb*PYK was found in the flowthrough, as expected because the pH of the eluting buffer (7.9) was similar to the theoretical pI of *Tb*PYK (7.74), resulting in a minimal net charge of the protein surface. Many of the contaminating *E. coli* proteins are charged at pH 7.9 and bind to the ion-exchange columns. Bound contaminants were eluted by a step of 40% elution buffer (50 m*M* TEA pH 7.9, 2 *M* KCl, 10% glycerol) for four CVs (80 ml) and were collected in 10 ml fractions, followed by a further cleaning step of at least two CVs of 100% elution buffer. The collected fractions were analysed by SDS–PAGE (Supplementary Fig. S2) and the flowthrough fractions containing *Tb*PYK were pooled and concentrated to 5 ml using a Vivaspin column (GE Healthcare, 100 kDa cutoff). The samples were then filtered through a 0.22 µm syringe filter and loaded onto a Superdex 200 pg XK 26/60 gel-filtration column pre-equilibrated with gel-filtration buffer (20 m*M* TEA pH 7.2, 50 m*M* KCl, 10 m*M* $MgCl_2$, 20% glycerol). The column (319 ml) was maintained at a constant flow rate of 2 ml min^{-1} throughout the purification process. The fractions containing *Tb*PYK eluted in a peak at ∼171 ml (corresponding to an apparent molecular mass of ∼220 kDa) and were analysed by SDS–PAGE. The verified pure (≥95%) *Tb*PYK samples were concentrated to 10 mg ml^{-1} and were stored at 193 K. The protein concentration was determined by measurement of the absorbance at 280 nm and was calculated using an extinction coefficient for *Tb*PYK of 17 880 M^{-1} cm^{-1}.

2.3. Enzyme-activity assay and kinetics study

The activity of *Tb*PYK was measured by following the decrease in NADH absorbance at 340 nm using a Molecular Devices M5 multimode plate reader and the *KaleidaGraph* software. One activity unit is defined as the conversion of 1 µmol substrate per minute under standard conditions. The assay was performed at 298 K in 100 µl reaction mixtures consisting of 50 m*M* TEA buffer pH 7.2, 50 m*M* KCl, 6 m*M* $MgCl_2$, 10% glycerol, 0.5 m*M* NADH and 5 µg (3.2 U) LDH. The reaction was initiated by the addition of diluted enzyme in 1× assay buffer (50 m*M* TEA pH 7.2, 50 m*M* KCl, 6 m*M* $MgCl_2$, 10% glycerol) to a final concentration of 1 µg ml^{-1}.

The specific activity of the enzyme was calculated from data obtained at saturated substrate concentrations (2.5 m*M* ADP and 10 m*M* PEP) for PYK. The turnover number (k_{cat}) of the enzyme was calculated from the enzyme specific activity divided by the subunit molar mass of 54 466.6 (g mol^{-1}). It is relevant to stress that all of the kinetic measurements were performed in the presence of $MgCl_2$ instead of $MgSO_4$ because of the known effects of sulfate on the conformation of *Lm*PYK (Tulloch *et al.*, 2008).

Enzyme kinetics with regard to ADP were studied with saturated PEP (10 m*M*) and at variable concentrations of ADP (from 0 to 2.5 m*M*). Enzyme kinetics with regard to PEP were studied with saturated ADP (2.5 m*M*) and at variable concentrations of PEP (from 0 to 10 m*M*) in the presence or absence of 1 µ*M* F26BP or in the presence or absence of 1 m*M* F16BP. When hyperbolic kinetics were obtained, the initial rates of NADH oxidation were determined and fitted to the Michaelis–Menten (M-M) equation: $V_0 = V^*_{max}[S]/(K_m + [S])$, where V_0 is the initial reaction rate, V_{max} is the maximum rate, [S] is the substrate concentration and K_m is the Michaelis constant of the investigated enzyme. When sigmoidal kinetics were obtained, the initial rates of NADH oxidation were determined and fitted to an extended M-M equation: $V_0 = V^*_{max}[S]^h/(S^h_{0.5} + [S]^h)$, where $S_{0.5}$ is the substrate concentration giving a half-maximal reaction rate and h is the Hill coefficient.

Enzyme kinetics with regard to the effector F16BP were studied at 2.5 m*M* ADP, 0.7 m*M* PEP and variable concentrations of F16BP. The initial reaction rates of NADH oxidation were determined and fitted to the equation $V'_0 = V'_{max}*[S]^h/(K^h_{a0.5} + [S]^h)$, where V'_0 is the initial reaction rate minus the initial rate in the absence of effector, V'_{max} is the maximum reaction rate minus the initial rate in the absence of effector, [S] is the concentration of effector, $K_{a0.5}$ is the activation (or inhibition) constant and h is the Hill coefficient.

2.4. Thermal shift assay

The assay involves monitoring changes in the fluorescence signal of SYPRO Orange dye as it interacts with a protein undergoing thermal unfolding. Test samples of 50 µl were assayed in a 96-well PCR plate (Bio-Rad) containing 50 m*M* TEA pH 7.2, 100 m*M* KCl, 10 m*M* $MgCl_2$, 10× SYPRO Orange dye [the dye is supplied by Invitrogen (catalogue No. S6650) at a 5000× concentration in DMSO and was diluted in assay buffer for use], 4 µ*M* enzyme and 10 m*M* of the test ligand PEP or oxalate. Buffer was added instead of test ligand in the negative-control samples. The temperature midpoint for the protein-unfolding transition (the melting temperature, T_m) was calculated using the Bio-Rad *iQ5* software. The plate was sealed with optical-quality sealing tape (Bio-Rad) and heated in an i-Cycler iQ5 real-time PCR detection system (Bio-Rad) from 293 to 353 K in increments of 1 K. Fluorescence changes in the wells were simultaneously monitored using a charge-coupled detector (CCD) camera. The wavelengths for excitation and emission were 485 and 575 nm, respectively.

2.5. Crystallization and data collection

Aliquots of the purified *Tb*PYK stocks (10 mg ml^{-1}) were used in the crystallization experiments. Frozen proteins were thawed on ice before use. Both cocrystallization and crystal-soaking experiments were performed by the vapour-diffusion method using the hanging-drop technique at 277 K. The drops were equilibrated against a reservoir filled with 1 ml well solution. To cocrystallize the enzyme *Tb*PYK and the activator F26BP, drops were set up by mixing 0.5 µl ligand solution and 1.5 µl well solution with 1 µl 10 mg ml^{-1} protein solution. The well solution consisted of 6–20% PEG 8000, 10–20% glycerol, 50 m*M* TEA buffer pH 7.2, 100 m*M* KCl, 50 m*M* $MgCl_2$. The final concentration of F26BP in the drops was 80 µ*M*. Crystals of *Tb*PYK–F26BP–Mg were grown in conditions consisting of 15–20% PEG 8000 plus 10–20% glycerol. To improve the diffraction quality of the crystals, the dye molecule Ponceau S was included in the drops at a final concentration of 800 µ*M* for cocrystallization; however, no electron density could be attributed to the dye molecule in the final electron-density maps.

For crystal-soaking experiments, a crystal of *Tb*PYK–F26BP–Mg was placed into a 2 µl drop of soaking solution composed of 5 m*M* PEP, 80 µ*M* F26BP, 800 µ*M* Ponceau S, 20% PEG 8000, 20% glycerol, 50 m*M* TEA buffer pH 7.2, 100 m*M* KCl, 50 m*M* $MgCl_2$. The drop harbouring the crystal was equilibrated overnight against a reservoir of 1 ml well solution consisting of 20% PEG 8000, 20% glycerol, 50 m*M* TEA buffer pH 7.2, 100 m*M* KCl, 50 m*M* $MgCl_2$.

X-ray intensity data were collected from crystals at the Diamond synchrotron-radiation facility in Oxfordshire, England. Intensity data for *Tb*PYK–F26BP–Mg and *Tb*PYK–F26BP–PEP were collected on the microfocus MX beamline I24 and beamline I04, respectively, from single crystals flash-cooled in liquid nitrogen at 100 K. Data were then processed with *MOSFLM* (Battye *et al.*, 2011) and scaled with *SCALA* (Evans, 2006). The data-collection and processing statistics are summarized in Table 1.

2.6. Structure determination

The *Tb*PYK–F26BP–Mg and the *Tb*PYK–F26BP–PEP–Mg structures were both solved by molecular replacement using the program *Phaser* (McCoy *et al.*, 2007). To determine the *Tb*PYK–F26BP–Mg structure, a monomer of *T. cruzi* PYK (PDB entry 3qv9; Morgan *et al.*, 2011) was used as a search model in a molecular-replacement experiment. Residues were then manually substituted to give the *Tb*PYK sequence and fitted into the density maps using *Coot* (Emsley & Cowtan, 2004). To determine the *Tb*PYK–F26BP–PEP–Mg structure, a monomer of the refined *Tb*PYK–F26BP–Mg structure was used as the search model in a molecular-replacement experiment.

In both structures, the B domain containing poor electron density was deleted from the structures at the beginning. The modified structures were subjected to five cycles of rigid-body refinement followed by five cycles of restrained refinement using *REFMAC* (Murshudov *et al.*, 2011). The side chains in

Table 1
Data-collection, refinement and Ramachandran plot statistics for *Tb*PYK–F26BP–Mg and *Tb*PYK–F26BP–PEP–Mg crystals.

Values in parentheses are for the highest resolution shell.

	*Tb*PYK–F26BP–Mg	*Tb*PYK–F26BP–PEP–Mg
Data collection and processing		
Space group	*I*222	*I*222
Unit-cell parameters (Å, °)	a = 103.68, b = 109.00, c = 268.38, $\alpha = \beta = \gamma$ = 90.00	a = 103.41, b = 108.93, c = 263.34, $\alpha = \beta = \gamma$ = 90.00
Solvent content (%)	65	64
Wavelength (Å)	0.98	0.98
Resolution (Å)	54.50–2.35	65.83–2.30
No. of reflections	411424 (60956)	536643 (78473)
No. of unique reflections	63644 (9232)	66318 (9572)
Wilson B factor (Å^2)	42.2	37.1
R_{merge} (%)	8.8 (54.6)	12.6 (67.0)
$\langle I/\sigma(I)\rangle$	12.4 (3.1)	11.3 (3.2)
R_{meas} (%)		
Within I+/I−	10.5 (64.8)	14.4 (76.7)
All I+ and I−	10.3 (64.2)	14.1 (75.9)
$R_{p.i.m.}$ (%)		
Within I+/I−	5.6 (34.4)	7.0 (37.1)
All I+ and I−	4.0 (24.6)	5.0 (26.3)
Completeness (%)	100.0 (100.0)	100.0 (100.0)
Multiplicity	6.5 (6.6)	8.1 (8.2)
Refinement statistics		
Monomers in asymmetric unit	2	2
No. of reflections	411424 (60417)	536643 (62951)
R_{work}/R_{free} (%)	16.38/19.87	14.62/18.84
No. of non-H atoms		
Total	8289	8594
Protein	7653	7666
Water	585	857
Ligands	51	71
Average B factors (Å^2)		
Overall	50.85	38.06
Overall (excluding B domain of chain A)	42.92	34.34
Protein (chain A and chain B)	51.60	37.56
Protein (chain A and chain B, excluding B domain of chain A)	43.02	33.27
B domain of chain A	130.59	76.11
B domain of chain B	56.87	44.02
Water	42.03	43.07
Ligands	39.71	32.39
No. of residues (protein)	994	996
No. of ligands	8	10
No. of waters	585	857
R.m.s. deviations		
Bond lengths (Å)	0.0104	0.0117
Bond angles (°)	0.9859	1.0976
Ramachandran plot		
Favoured (%)	97.2	97.2
Allowed (%)	99.8	99.8
No. of outliers†	2	2

† The outlier residue in each monomer is Thr296, a key active-site residue that is commonly found in this configuration in PYK structures.

the models were then manually adjusted using *Coot*, followed by several cycles of restrained refinement using *REFMAC*. Where appropriate, ligands (F26BP, K^+, Mg^{2+} or PEP) and water molecules were added to the structure. After further cycles of restrained refinement and manual adjustments to side chains, ligands and water molecules, the overall quality of the map improved and the electron density for the missing B domain became clearer. The missing B domain was then built manually using *Coot* followed by cycles of TLS and restrained refinement and *Coot* adjustments. Ten TLS groups were generated according to the domain regions of PYK and consisted of residues 2–14 (chain *A*), residues 15–87 (chain *A*), residues 88–189 (chain *A*), residues 190–357 (chain *A*), residues 358–499 (chain *A*), residues 2–14 (chain *B*), residues 15–87 (chain *B*), residues 88–189 (chain *B*), residues 190–357 (chain *B*) and residues 358–499 (chain *B*). The figures were generated using *PyMOL* (DeLano, 2002). The data-processing and refinement statistics are summarized in Table 1.

Superpose (Krissinel & Henrick, 2004) from *CCP*4 (Winn *et al.*, 2011) was used to calculate the allosteric rigid-body rotations from the superposition of T-state and R-state tetramers as described previously (Morgan *et al.*, 2010). Both r.m.s. differences and rotation matrices were calculated in the superposition process.

The structure factors and coordinates for *Tb*PYK–F26BP–Mg and *Tb*PYK–F26BP–PEP–Mg have been deposited in the RCSB Protein Data Bank as PDB entries 4hyw and 4hyv, respectively.

3. Results and discussion

3.1. Purification and characterization of *Tb*PYK

A codon-optimized gene was used to overexpress untagged *Tb*PYK in *E. coli* BL21(DE3) cells. Two ion-exchange purification steps followed by gel filtration gave soluble protein with a final yield of up to 60 mg per litre of culture (see §2).

The overall kinetic properties of purified *Tb*PYK are similar to, but distinct from, those of PYK from *L. mexicana* (Table 2). In the absence of effector, *Tb*PYK displays sigmoidal kinetics with respect to its substrate PEP, with an apparent affinity $S_{0.5}$ of 1.03 (±0.08) m*M* and a Hill coefficient (h) of 1.88 (±0.12), indicating positive cooperativity. F26BP has been shown to be the natural allosteric effector for trypanosomatid PYKs, with affinities in the nanomolar range (Barnard & Pedersen, 1988; Callens *et al.*, 1991; Callens & Opperdoes, 1992; Ernest *et al.*, 1994, 1998). The presence of F26BP increases the apparent PEP-binding affinity of *Tb*PYK from 1.03 (±0.08) to 0.119 (±0.026) m*M*, making the PEP saturation curve almost hyperbolic (Table 2). The presence of fructose 1,6-bisphosphate (F16BP; the natural activator for mammalian, yeast

Table 2
Comparison of the kinetic properties of *Tb*PYK and *Lm*PYK.

n.d., not determined.

Ligand	Modulator	Kinetic parameter	*Tb*PYK†	*Tb*PYK‡	*Tb*PYK§	*Lm*PYK¶
PEP	None	$S_{0.5}$ (m*M*)	1.03 ± 0.08	1.48	1.28	1.44 ± 0.28
		h††	1.88 ± 0.12	2.40	3.20	2.81 ± 0.52
		k_{cat} ($min^{-1} \times 10^{-3}$)	8.72 ± 0.16	33.6	20.3	21.0 ± 1.5
		$k_{cat}/S_{0.5}$ ($mM^{-1}\ min^{-1} \times 10^{-3}$)	8.49	22.7	15.8	14.6
	F26BP	$S_{0.5}$ (m*M*)	0.119 ± 0.026	0.15	0.055	0.195 ± 0.004
		h	1.19 ± 0.10	1.00	1.00	2.72 ± 0.70
		k_{cat} ($min^{-1} \times 10^{-3}$)	13.9 ± 0.26	28.6 ± 0.7	19.0	11.0 ± 0.6
		$k_{cat}/S_{0.5}$ ($mM^{-1}\ min^{-1} \times 10^{-3}$)	117	191	344	56.4
	F16BP	$S_{0.5}$ (m*M*)	0.261 ± 0.040	0.460	n.d.	0.840 ± 0.003
		h	1.31 ± 0.09	1.40	n.d.	2.68 ± 0.37
		k_{cat} ($min^{-1} \times 10^{-3}$)	11.1 ± 0.23	31.0	n.d.	25.0 ± 0.1
		$k_{cat}/S_{0.5}$ ($mM^{-1}\ min^{-1} \times 10^{-3}$)	42.7	67.4	n.d.	29.8
ADP	None	K_m (m*M*)	0.136 ± 0.028	0.114 ± 0.013	0.109 ± 0.048	0.264 ± 0.007
		k_{cat} ($min^{-1} \times 10^{-3}$)	8.92 ± 0.22	n.d.	16.9 ± 0.502	8.95 ± 0.31
		k_{cat}/K_m ($mM^{-1}\ min^{-1} \times 10^{-3}$)	65.8	n.d.	155	33.9
F26BP	None	$K_{a0.5}$ (μ*M*)	n.d.	0.0560 ± 0.002	0.0130 ± 0.006	0.290 ± 0.001
F16BP	None	$K_{a0.5}$ (m*M*)	0.0470 ± 0.029	0.121 ± 0.003	0.0260 ± 0.009	0.520 ± 0.211

† Untagged version expressed in *E. coli* (this work); assayed in the presence of $MgCl_2$ instead of $MgSO_4$. ‡ Purified from bloodstream-form parasites (Callens *et al.*, 1991; Barnard & Pedersen, 1988; Callens & Opperdoes, 1992). § Untagged version expressed in *E. coli* (Ernest *et al.*, 1998). ¶ Untagged version expressed in *E. coli* (Ernest *et al.*, 1994). †† The Hill coefficient.

and bacterial PYKs) also increases the apparent PEP-binding affinity of *Tb*PYK to 0.261 (±0.040) m*M* and decreases *h* to 1.31 (±0.10), indicating decreased cooperativity. *Tb*PYK has a micromolar affinity of 47 μ*M* for F16BP, which is similar to previously reported data for *Tb*PYK (Table 2). The apparently approximately tenfold weaker affinity of *Lm*PYK for F16BP and F26BP may be a consequence of the sensitivity of this enzyme to the presence of sulfate (Tulloch *et al.*, 2008) in the assay conditions (Ernest *et al.*, 1994).

From the data in Table 2, it is clear that in the presence of either F26BP or F16BP the k_{cat} values for the reactions where PEP is the varied substrate are significantly higher than for the reaction in the absence of the allosteric activators. This does not fit the simple model of K-system allostery in which the R state has a higher affinity for the substrate but k_{cat} remains constant. We have recently shown that the human M2PYK isoform exists in a monomer–tetramer equilibrium and enzymatic activity is regulated in part by its ability to dissociate into inactive monomers, resulting in V-type kinetics (Morgan *et al.*, 2013). The lower k_{cat} values for *Tb*PYK in the absence of effector suggest that a similar mechanism may be at work in *Tb*PYK and may explain the observed V-type allosteric enzyme kinetics.

3.2. The structures of *Tb*PYK–F26BP–Mg with and without PEP

Previously, the only available crystal structure of any PYK with its physiological activator but without active-site ligands was the low-resolution (5 Å) structure of an *Lm*PYK–F26BP complex (Morgan *et al.*, 2010). Here, we report the F26BP-bound *Tb*PYK crystal structure (*Tb*PYK–F26BP–Mg) at a resolution of 2.35 Å (Table 1). The dye Ponceau S was used in the crystallization conditions as an additive to improve the crystal packing, as previously observed for other sulfonic acid-containing dyes (Morgan *et al.*, 2011). Without this additive, a different crystal form with three tetramers per asymmetric unit was obtained that only diffracted to 2.95 Å resolution. As well as the substrate-free structure, a *Tb*PYK–F26BP–PEP–Mg complex was also obtained by soaking PEP into the *Tb*PYK–F26BP–Mg crystals (Table 1).

The *Tb*PYK–F26BP–Mg and the *Tb*PYK–F26BP–Mg–PEP X-ray crystal structures show the expected tetrameric architecture (Fig. 1*a*), which is similar to the published *Lm*PYK R-state structure (PDB entry 3hqp; Morgan *et al.*, 2010). The average C^{α} r.m.s. differences between the R-state tetrameric structures of *Tb*PYK and *Lm*PYK are less than 1 Å for the AC cores (Table 3). The transition between the R and T states requires a concerted rigid-body rotation of each of the four AC cores in the tetramer. In contrast, a fit of the *Tb*PYK–F26BP–Mg or the *Tb*PYK–F26BP–Mg–PEP structure onto the AC core of the T-state apoenzyme *Lm*PYK (PDB entry 3hqn) structure shows greater r.m.s. differences (2.5 Å) and is a consequence of a rigid-body rotation with an angle of 8.3° (Supplementary Table S2).

The B domains of the two crystallographically independent chains of the *Tb*PYK–F26BP–Mg structure show closely similar orientations; however, there is a significant difference in temperature factors, with average values of 130 and 56 $Å^2$ for the B domains of chains *A* and *B*, respectively, compared with an average *B* factor of 51 $Å^2$ for the tetramer (Table 1). Differences between the two crystallographically independent chains of the two-chain asymmetric unit is a common feature of PYK structures and will be considered in more detail in §3.5.

Ligand binding also has a very marked effect on the thermal stability of *Tb*PYK (§2.4). Unligated (T-state) *Tb*PYK has a T_m of 319 K and the addition of PEP or oxalate increases the T_m by over 15 K to 337 and 336 K, respectively. These results

Table 3
Average r.m.s. differences (Å) between PYK tetrameric structures (AC cores).

	*Tb*PYK–F26BP–Mg	*Tb*PYK– F26BP–PEP–Mg
*Tb*PYK–F26BP–Mg	0	0.20
*Tb*PYK–F26BP–PEP–Mg	0.20	0
*Lm*PYK–F26BP–OX–ATP (PDB entry 3hqp)	0.82	0.87
Apo *Lm*PYK (PDB entry 3hqn)	2.54	2.52

correlate well with the very significant ligand-induced structural changes which occur during B-domain closure as well as the transition between the T and R states.

3.3. The effector-binding site of *Tb*PYK

The F26BP effector molecule is held in place by a network of salt bridges and hydrogen bonds (Figs. 2*b* and 2*c*). In both of the crystallographically independent F26BP-binding sites, the 2′-phospho group interacts with Lys454 and Arg457 (residue numbers throughout this paper refer to *Tb*PYK, unless indicated otherwise) with an additional direct hydrogen bond to the side chain of Asn402. The 6′-phospho group makes direct hydrogen bonds to the side chains and backbones of Ser401, Asn402, Thr403, Arg405 and Ser406. Additionally, some interactions are mediated by water-molecule networks involving Asn402, Glu450, Lys454, Lys487 and Gly488.

The residues that are involved in F26BP binding are highly conserved between trypanosomatid PYKs, but show much lower conservation compared with the mammalian, yeast and bacterial PYKs that are activated by F16BP (Fig. 2*a*). Similar to the R-state structure of *Lm*PYK (Morgan *et al.*, 2010), a conserved salt bridge (Asp483–Arg494) is formed across the C–C interface as a result of the stabilization of the loop by the binding of F26BP, which helps to lock the enzyme in its active state. Despite considerable efforts from various laboratories, no well diffracting crystals of a complex of FBP with pyruvate kinase have previously been obtained without an additional substrate analogue or nucleotide binding at the active site. The *Tb*PYK–F26BP–Mg structure presented here shows for the first time that the presence of FBP and Mg^{2+} alone are sufficient to stabilize the tetramer in an active R-state conformation.

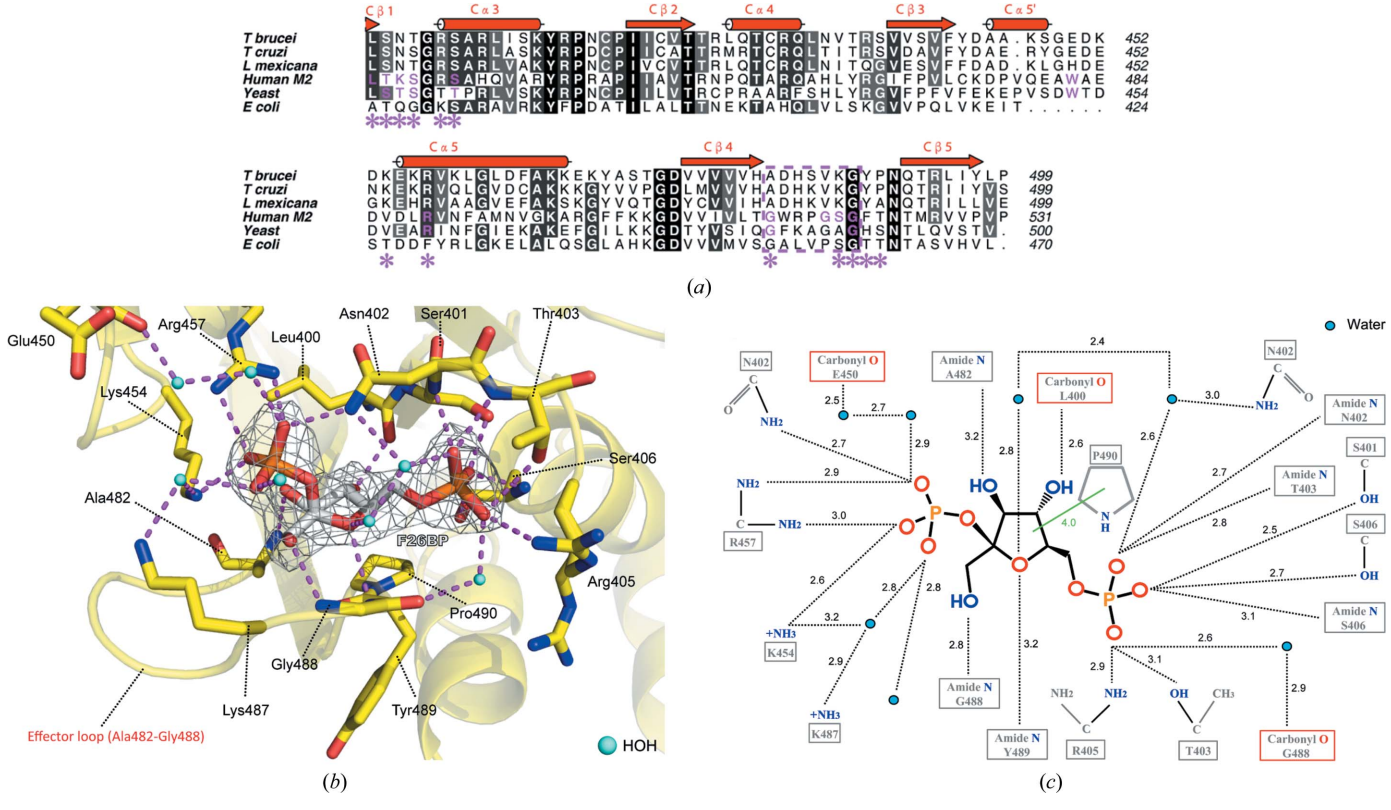

Figure 2
The effector site of *Tb*PYK with bound F26BP. (*a*) Sequence alignment of pyruvate kinases from *T. brucei*, *T. cruzi*, *L. mexicana*, human (M2), *Saccharomyces cerevisiae* and *E. coli* (starting from residue 400 of *Tb*PYK; Goujon *et al.*, 2010; Sievers *et al.*, 2011). Secondary-structural elements were defined by *DSSP* (Kabsch & Sander, 1983; Joosten *et al.*, 2011). Black, identical in five or six sequences; grey, conserved in four sequences; white, low conservation. The figure was generated using the program *ALINE* (Bond & Schüttelkopf, 2009). In *Tb*PYK, the amino acids involved in effector F26BP binding are indicated by asterisks. The amino acids involved in effector F16BP binding in human M2PYK and yeast PYK are coloured pink. The effector-loop residues are indicated by a pink dashed box. (*b*) Close-up of the effector site of *Tb*PYK–F26BP–Mg. The F26BP molecule is shown with an unbiased $F_o - F_c$ electron-density map contoured at 5.0σ (grey). Water molecules are shown as cyan spheres. Interactions (within 3.2 Å) are indicated by dashed lines in pink. (*c*) Schematic drawing showing the interactions at the *Tb*PYK effector site.

3.4. Protein–ligand interactions at the PEP-binding site

PEP binds in the *Tb*PYK–F26BP–PEP–Mg structure in a similar position at the active site (Fig. 3*a*) as the previously reported substrate analogues bound to other PYKs from a variety of species, including oxalate (Larsen *et al.*, 1998; Dombrauckas *et al.*, 2005; Christofk *et al.*, 2008; Morgan *et al.*, 2010), pyruvate (Larsen *et al.*, 1994; Wooll *et al.*, 2001; Williams *et al.*, 2006; Fenton *et al.*, 2010), phospholactate (Larsen *et al.*, 1997) and phosphoglycolate (Jurica *et al.*, 1998; Valentini *et al.*, 2002). The Mg^{2+} is coordinated by the phospho and carboxyl groups of PEP and by the carboxyl groups of residues Asp265 and Glu241 as well as one water molecule (Figs. 3*a* and 3*b*) in the Mg-1 canonical binding site. The octahedral coordination geometries of Mg^{2+} in the two crystallographically independent chains of *Tb*PYK–F26BP–PEP–Mg are shown in Supplementary Figs. S3(*a*) and S3(*b*). The monovalent K^+ also coordinates directly with the phospho group of PEP and forms a distorted octahedral coordination sphere which is similar to that of the structure of the PEP-free complex (*Tb*PYK–F26BP–Mg), but one coordinating water molecule is replaced by the O atom of the phospho group of PEP (Supplementary Figs. S3*c* and S3*d*). The carboxyl group of PEP forms interactions with the small α-helix Aα6′ and with the side chain of Thr297. An overlay of the structure of rabbit muscle M1PYK complexed with L-phospholactate (Larsen *et al.*, 1997) with that of *Tb*PYK–F26BP–PEP–Mg shows a reasonable (∼2 Å) correspondence of the carboxyl groups of PEP and L-phos-

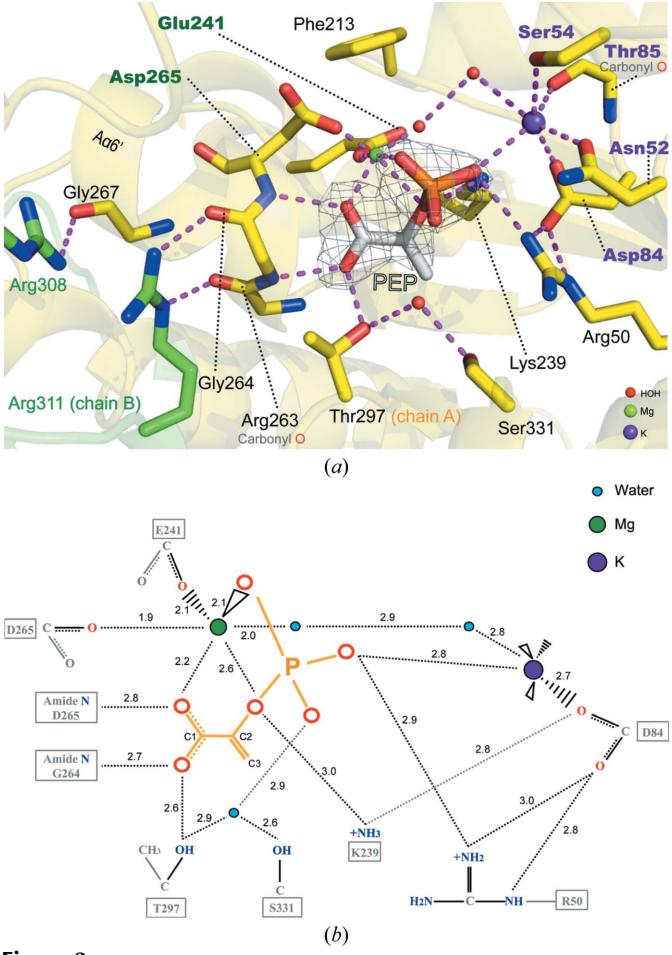

Figure 3
The active site of *Tb*PYK with bound PEP. (*a*) Chain *A* of the PYK tetramer is coloured yellow and chain *B* is coloured green. The divalent metal ion Mg^{2+} is shown as a green sphere. The monovalent ion K^+ is shown as a purple sphere and is coordinated by the residues labelled in purple. Water molecules are shown as red spheres. The $F_o - F_c$ electron density for the substrate PEP molecule is shown as a grey mesh contoured at 5.0σ. Hydrogen bonds are indicated by pink dashed lines. (*b*) Schematic drawing showing the interactions at the *Tb*PYK–F26BP–PEP–Mg active site (chain *A*) and including $F_o - F_c$ electron density for the metal ions.

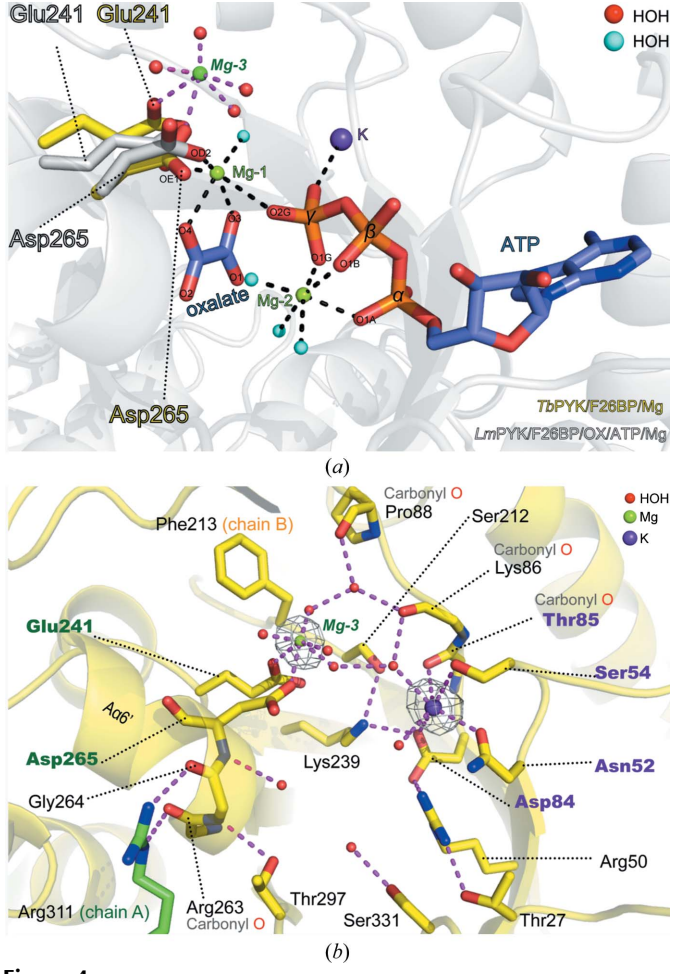

Figure 4
Comparison of the active sites of *Lm*PYK–F26BP–OX–ATP–Mg (PDB entry 3hqp) and *Tb*PYK–F26BP–Mg. (*a*) *Lm*PYK–F26BP–OX–ATP–Mg active site (white) showing Mg-1, Mg-2, oxalate and ATP. The two Mg-coordinating residues (Glu241 and Asp265), oxalate and ATP are shown in stick representation. Mg-1 coordinates to Glu241 and Asp265, oxalate (O3 and O4), ATP (O2G) and one water molecule (cyan sphere). Mg-2 coordinates to the α-, β- and γ-phospho groups of ATP and three water molecules. *Tb*PYK–F26BP–Mg was superposed and Mg-3 together with coordinating residues Glu241 and Asp265 (yellow) and coordinating water molecules (red spheres) from this structure are shown. (*b*) Close-up of the active site of *Tb*PYK–F26BP–Mg with chain *B* coloured yellow and chain *A* coloured green. The short α-helix Aα6′ (residues Arg263–Glu269) forms two hydrogen bonds to the side chain of residue Arg311 from the neighbouring subunit. Mg^{2+}, K^+ and water molecules are shown as green, purple and red spheres, respectively. The $F_o - F_c$ electron densities for Mg^{2+} and K^+ are contoured at 4.0σ. Interatomic interactions (within 3.3 Å) are indicated by pink dashed lines.

Table 4
Summary of B-domain positions in trypanosomatid PYK structures.

PYK structure	PDB code	State	Chains in asymmetric unit	B domains in tetramer
*Tb*PYK–F26BP–Mg	4hyw	R	2	Chains *A* and *D*, open, *B* factor 130 Å^2; chains *B* and *C*, open, *B* factor 56 Å^2
*Tb*PYK–F26BP–PEP–Mg	4hyv	R	2	Chains *A* and *D*, partly closed; chains *B* and *C*, open
*Lm*PYK–F26BP–OX–ATP	3hqp	R	16	All chains closed
*Tc*PYK–Ponceau S	3qv9	T	2	Chains *A* and *D*, open; chains *B* and *C*, disordered

pholactate, but a closer (∼1 Å) fit of the phospho groups. In both structures the phospho group interacts with Arg50 and Lys239 (Arg72 and Lys269 in rabbit muscle M1PYK), which are conserved even among diverse species (Supplementary Fig. S1) and may play an essential role in phospho transfer.

3.5. Crystal soaking with substrate induces a large B-domain movement

The two structures described here, *Tb*PYK–F26BP–Mg and *Tb*PY–KF26BP–PEP–Mg, provide a unique example of large-scale '*in crystallo*' domain movements induced by soaking the substrate into the crystal. The program *DynDom* (Hayward *et al.*, 1997; Hayward & Berendsen, 1998) was used to analyse these movements and Fig. 1(*b*) shows the 23° rotation of the B domain with respect to the AC core induced by PEP binding. It is apparent that in the presence of F26BP 5 m*M* PEP is sufficient to cause partial domain closure. Only one of the two crystallographically independent B domains shows this movement, as crystal-packing interactions lock the other B domain in an open conformation. The

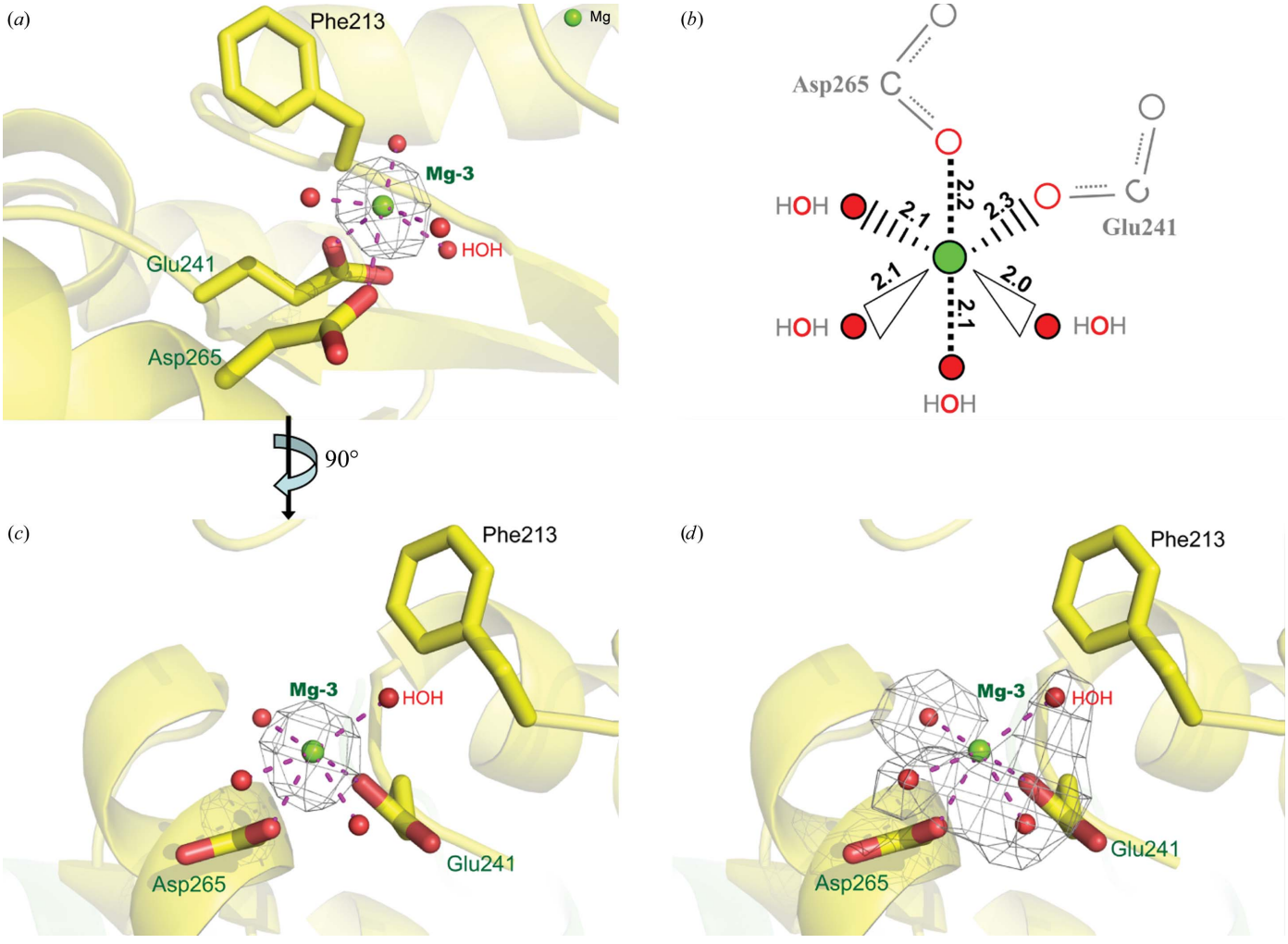

Figure 5
Close-up of the Mg-coordination site Mg-3 adjacent to the active site of *Tb*PYK–F26BP–Mg (chain *B*). (*a*, *c*) Orthogonal views of the Mg-coordination site. Mg-3 and water molecules are shown as green spheres and red spheres, respectively. The $F_o - F_c$ electron density for Mg^{2+} is contoured at 4.0σ. (*b*) Schematic representation of the coordination sphere of Mg^{2+}. The interatomic distances are given in Å. (*d*) The $F_o - F_c$ electron density for water molecules involved in Mg coordination contoured at 3.5σ.

conformation of the B domain observed in chain *A* can be classified as half-closed. Fully closed B-domain conformations (Fig. 1*b*) differ in rotation angle by about 40° compared with open-form structures (Larsen *et al.*, 1998; Morgan *et al.*, 2010) and have only been observed in PYK structures with bound ATP. Attempts at soaking in nucleotides were not successful; crystals of *Tb*PYK–F26BP–Mg soaked in an equimolar mixture of PEP and ADP showed only PEP bound.

A common feature of trypanosomatid PYK crystal structures is the occurrence of two crystallographically distinct chains in the asymmetric unit. One asymmetric unit corresponds to chains *A* and *B* in Fig. 1(*a*) (which are related by a crystallographic twofold axis to chains *D* and *C*, respectively). In other published structures the B domains of two crystallographically independent chains frequently adopt different conformations which are presumably the result of different crystal-packing environments. Table 4 summarizes the distinct conformations of the chains of the four trypanosomatid PYK structures described in this paper. Only in the fully ligated *Lm*PYK structure do all four chains have identical conformations in which the B domains adopt the fully closed position.

3.6. A third Mg^{2+}-binding site is revealed adjacent to the active site of R-state *Tb*PYK in the absence of substrates

Divalent metal ions are essential for phospho transfer during the catalytic cycle of PYKs, where Mg^{2+} is generally considered to be the physiologically relevant metal. Fig. 4(*a*) shows the positions of the two canonical Mg^{2+} ions (Mg-1 binds oxalate and Mg-2 binds to ATP by tridentate interactions) found in PYK structures crystallized with a variety of nonproductive ligand mixtures (Larsen *et al.*, 1994, 1997, 1998; Jurica *et al.*, 1998; Wooll *et al.*, 2001; Valentini *et al.*, 2002; Dombrauckas *et al.*, 2005; Christofk *et al.*, 2008; Fenton *et al.*, 2010; Morgan *et al.*, 2010). The Mg-2 position is only observed in structures that contain ATP (Larsen *et al.*, 1998; Morgan *et al.*, 2010). Divalent metal ions have never been found in T-state PYK structures, although divalent metal ions were present at relatively high concentrations in the buffers from which the PYKs were crystallized (Mattevi *et al.*, 1995; Rigden *et al.*, 1999; Morgan *et al.*, 2010, 2011).

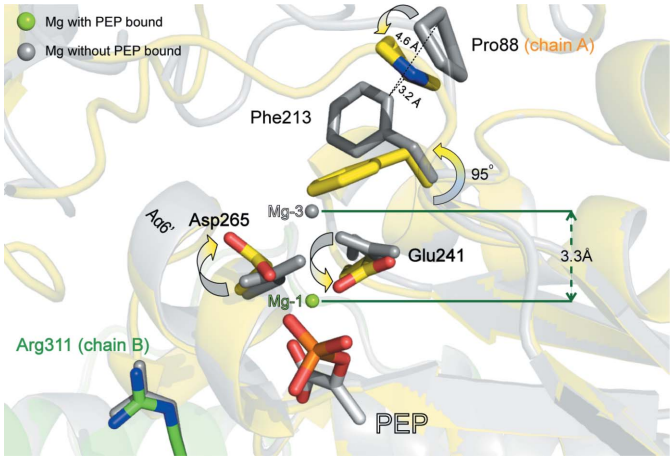

Figure 6
Changes at the active site of *Tb*PYK on PEP binding. *Tb*PYK–F26BP–PEP–Mg (yellow, chain *A*; green, chain *B*; white, substrate PEP) is shown superposed on *Tb*PYK–F26BP–Mg (grey side chains). The two Mg^{2+} positions are shown as spheres, with the grey sphere in the 'priming' position (Mg-3 position) and the green sphere in the canonical position (Mg-1 position) for coordination to PEP. The distance between these two Mg^{2+} ions is 3.3 Å. The reorientations of the side chain of Phe213 and the carboxyl side chains of residues Asp265 and Glu241 are indicated by arrows. The small movement of Pro88 is also shown. The distances between Pro88 and Phe213 are shown as black dotted lines.

The crystal structure of *Tb*PYK–F26BP–Mg that we report here shows for the first time the presence of Mg^{2+} (Mg-3) in a site adjacent to the active site of R-state PYK in the absence of substrates or substrate analogues (Fig. 4*b*). Interestingly, this Mg-3 binding site is distinct from both of the previously described canonical positions and lies ∼3 Å away from the canonical Mg-1 position (Fig. 4*a*). It is nevertheless coordinated by the same side-chain carboxyl groups of Glu241 and Asp265, requiring that these side chains adopt different conformational poses, as discussed in the next section. The distorted octahedral coordination geometry around this Mg-3 site is formed by interactions with the two negatively charged side chains and four water molecules (Fig. 4*b* and 5) and is fully consistent with the presence of Mg^{2+}. The coordinating distances of the Mg^{2+} at the Mg-3 binding site of *Tb*PYK–F26BP–Mg range from 2.0 to 2.3 Å.

3.7. Changes in Mg^{2+} coordination are required for closure of the B domain

Superposition of the active sites of the *Tb*PYK–F26BP–Mg and *Tb*PYK–F26BP–PEP–Mg structures (Fig. 6) reveals the concerted movements that occur when the PEP substrate binds. The movement of Mg^{2+} from the Mg-3 location to the PEP-coordinated Mg-1 location correlates with a number of side-chain conformational changes. As well as the rotation of the side chains of Asp265 and Glu241 (described above), there is a large side-chain movement of Phe213, in which the dihedral angle is rotated by 95° to fill the vacated Mg-3 space (Fig. 6). Interestingly, the structure of the constitutively active rabbit muscle M1PYK cocrystallized with L-phospholactate also showed a range of open and partially closed B-domain conformations, with Mg^{2+} coordination to the phospho group lacking when the B domain was in the open conformation (Larsen *et al.*, 1997). In this conformation with bound L-phospholactate the Mg^{2+} was instead located at a site adjacent to the active site in a similar position to Mg-3 observed in *Tb*PYK in the presence of F26BP but in the absence of PEP. In this way, the structure of the constitutively active rabbit muscle M1PYK in the presence of a substrate analogue can resemble the structure of the effector-activated *Tb*PYK in the absence of substrate.

The open and closed X-ray structures presented here (Figs. 1*b*, 6 and 7) show that substrate binding correlates with three structural (and presumably closely synchronous) changes: a gross domain movement of the B domain, a change in magnesium-ion coordination and a series of concerted side-

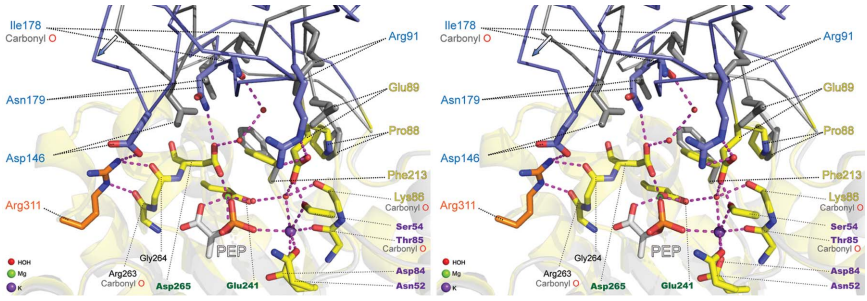

Figure 7
Stereo image of the superposed active sites of the partially closed chain *A* of *Tb*PYK–F26BP–PEP–Mg (blue) and the open chain *B* (grey) of *Tb*PYK–F26BP–Mg showing the interactions involved in B-domain movement. The interacting residues and PEP are shown as sticks, while metal ions and water molecules are shown as spheres. The interatomic interactions (within 3.2 Å) which occur upon PEP binding and B-domain closure are indicated as pink dashed lines.

chain movements. The phenyl group of Phe213 rotates away from Pro88 and allows movement of Pro88, which sits in the middle of a linker strand tethering the B domain to the A domain. When the B domain is in its closed conformation a series of strong interdomain hydrogen bonds are formed (Arg311 to Asp146 and Asp265 to Asn179, as shown in Fig. 7).

3.8. Mg^{2+} collaborates with FBP as a natural activator of PYK

Binding of F26BP stabilizes the R-state (active) conformation of trypanosomatid PYKs, which allows more efficient binding of PEP ($S_{0.5}$ = 0.119 m*M*) compared with T-state PYK ($S_{0.5}$ = 1.03 m*M*) (Table 2). This difference in binding can be rationalized by subtle structural differences at their active sites (Morgan *et al.*, 2010): the flexible Aα6′ helix is held rigid in an ideal binding geometry for the substrate in the R-state structure, while the Aα6′ helix in the T-state structure adopts a slightly different conformation with a less optimal geometry for binding substrate (Supplementary Fig. S4). Interestingly, although the T-state structure was crystallized in the presence of 50 m*M* Mg^{2+}, no ions were located in the active site. In contrast, in both R-state structures presented here we see that Mg^{2+} (both in the canonical PEP-bound Mg-1 position and in the Mg-3 or 'priming' position) coordinates in such a way as to stabilize the R-state active-site conformation (Figs. 4 and 6). This suggests that both the effector molecule F26BP and the magnesium ions stabilize the R-state conformation and that Mg^{2+} plays an additional role in the allosteric mechanism over and above its catalytic function. Such a hypothesis is consistent with published results showing that *Tb*PYK has a sigmoidal response in activity with respect to Mg^{2+}, Mn^{2+} and Co^{2+} concentration (Callens *et al.*, 1991). It is noteworthy that in our crystallization trials crystals never grew in the presence of F26BP without Mg^{2+}, which indicates that *Tb*PYK might not be able to adopt a stable R-state structure with F26BP alone. In contrast, crystals of the *Tb*PYK–F26BP–Mg complex grew readily in the presence of the metal. Similar observations have been made with yeast PYK, which shows enhanced binding of its natural effector F16BP in the presence of Mn^{2+} (Mesecar & Nowak, 1997*a*,*b*).

3.9. Mg^{2+} and K^{+} are retained at or near the active site of PYK in the presence of FBP to facilitate PEP binding

The comparison of the *Tb*PYK–F26BP–Mg and *Tb*PYK–F26BP–PEP–Mg structures shows that when PEP binds there is a reorientation of the side chains of Phe213, Asp265 and Glu241 such that the Mg^{2+} ion moves 3.3 Å from the Mg-3 pocket to coordinate to the phospho group of PEP and occupy the canonical Mg-1 pocket (Figs. 4 and 6). It is tempting to suggest that these two Mg^{2+}-binding sites play important roles in both substrate recognition (by maintaining the active-state conformation) and product release (by regulating the opening and closing of the B domain). By retaining and sequestering both Mg^{2+} (as observed in the Mg-3 site of *Tb*PYK–F26BP–Mg) and K^{+}, the enzyme would maintain its active R-state conformation and the active site would be primed to accept the next PEP substrate molecule.

This research was supported by the MRC, the Wellcome Trust, the Scottish University Life Sciences Alliance and the BBSRC. The Centre for Translational and Chemical Biology and the Edinburgh Protein Production Facility (EPPF) were funded by the Wellcome Trust and the BBSRC. We are grateful to Dr David A. Okar at the Veterans Administration Medical Centre (USA) for the gift of F26BP, to Dr Martin Wear and his colleagues at EPPF and to the staff at the synchrotron facility at Diamond, UK.

References

Albert, M. A., Haanstra, J. R., Hannaert, V., Van Roy, J., Opperdoes, F. R., Bakker, B. M. & Michels, P. A. M. (2005). *J. Biol. Chem.* **280**, 28306–28315.
Baker, N., Glover, L., Munday, J. C., Aguinaga Andrés, D., Barrett, M. P., de Koning, H. P. & Horn, D. (2012). *Proc. Natl Acad. Sci. USA*, **109**, 10996–11001.
Barnard, J. P. & Pedersen, P. L. (1988). *Mol. Biochem. Parasitol.* **31**, 141–147.
Battye, T. G. G., Kontogiannis, L., Johnson, O., Powell, H. R. & Leslie, A. G. W. (2011). *Acta Cryst.* D**67**, 271–281.
Bond, C. S. & Schüttelkopf, A. W. (2009). *Acta Cryst.* D**65**, 510–512.
Callens, M., Kuntz, D. A. & Opperdoes, F. R. (1991). *Mol. Biochem. Parasitol.* **47**, 19–29.
Callens, M. & Opperdoes, F. R. (1992). *Mol. Biochem. Parasitol.* **50**, 235–243.
Christofk, H. R., Vander Heiden, M. G., Wu, N., Asara, J. M. & Cantley, L. C. (2008). *Nature (London)*, **452**, 181–186.
DeLano, W. L. (2002). *PyMOL*. http://www.pymol.org.
Dombrauckas, J. D., Santarsiero, B. D. & Mesecar, A. D. (2005). *Biochemistry*, **44**, 9417–9429.
Emsley, P. & Cowtan, K. (2004). *Acta Cryst.* D**60**, 2126–2132.
Ernest, I., Callens, M., Opperdoes, F. R. & Michels, P. A. M. (1994). *Mol. Biochem. Parasitol.* **64**, 43–54.
Ernest, I., Callens, M., Uttaro, A. D., Chevalier, N., Opperdoes, F. R., Muirhead, H. & Michels, P. A. M. (1998). *Protein Expr. Purif.* **13**, 373–382.
Evans, P. (2006). *Acta Cryst.* D**62**, 72–82.

Fenton, A. W., Johnson, T. A. & Holyoak, T. (2010). *Protein Sci.* **19**, 1796–1800.
Flynn, I. W. & Bowman, I. B. (1980). *Arch. Biochem. Biophys.* **200**, 401–409.
Goujon, M., McWilliam, H., Li, W., Valentin, F., Squizzato, S., Paern, J. & Lopez, R. (2010). *Nucleic Acids Res.* **38**, W695–W699.
Hayward, S. & Berendsen, H. J. C. (1998). *Proteins*, **30**, 144–154.
Hayward, S., Kitao, A. & Berendsen, H. J. C. (1997). *Proteins*, **27**, 425–437.
Joosten, R. P., te Beek, T. A., Krieger, E., Hekkelman, M. L., Hooft, R. W. W., Schneider, R., Sander, C. & Vriend, G. (2011). *Nucleic Acids Res.* **39**, D411–D419.
Jurica, M. S., Mesecar, A., Heath, P. J., Shi, W., Nowak, T. & Stoddard, B. L. (1998). *Structure*, **6**, 195–210.
Kabsch, W. & Sander, C. (1983). *Biopolymers*, **22**, 2577–2637.
Krissinel, E. & Henrick, K. (2004). *Acta Cryst.* D**60**, 2256–2268.
Larsen, T. M., Benning, M. M., Rayment, I. & Reed, G. H. (1998). *Biochemistry*, **37**, 6247–6255.
Larsen, T. M., Benning, M. M., Wesenberg, G. E., Rayment, I. & Reed, G. H. (1997). *Arch. Biochem. Biophys.* **345**, 199–206.
Larsen, T. M., Laughlin, L. T., Holden, H. M., Rayment, I. & Reed, G. H. (1994). *Biochemistry*, **33**, 6301–6309.
Mattevi, A., Valentini, G., Rizzi, M., Speranza, M. L., Bolognesi, M. & Coda, A. (1995). *Structure*, **3**, 729–741.
McCoy, A. J., Grosse-Kunstleve, R. W., Adams, P. D., Winn, M. D., Storoni, L. C. & Read, R. J. (2007). *J. Appl. Cryst.* **40**, 658–674.
Mesecar, A. D. & Nowak, T. (1997*a*). *Biochemistry*, **36**, 6792–6802.
Mesecar, A. D. & Nowak, T. (1997*b*). *Biochemistry*, **36**, 6803–6813.
Morgan, H. P., McNae, I. W., Nowicki, M. W., Hannaert, V., Michels, P. A. M., Fothergill-Gilmore, L. A. & Walkinshaw, M. D. (2010). *J. Biol. Chem.* **285**, 12892–12898.
Morgan, H. P., McNae, I. W., Nowicki, M. W., Zhong, W., Michels, P. A. M., Auld, D. S., Fothergill-Gilmore, L. A. & Walkinshaw, M. D. (2011). *J. Biol. Chem.* **286**, 31232–31240.
Morgan, H. P., O'Reilly, F. J., Wear, M. A., O'Neill, J. R., Fothergill-Gilmore, L. A., Hupp, T. & Walkinshaw, M. D. (2013). *Proc. Natl Acad. Sci. USA*, **110**, 5881–5886.
Murshudov, G. N., Skubák, P., Lebedev, A. A., Pannu, N. S., Steiner, R. A., Nicholls, R. A., Winn, M. D., Long, F. & Vagin, A. A. (2011). *Acta Cryst.* D**67**, 355–367.
Rigden, D. J., Phillips, S. E., Michels, P. A. M. & Fothergill-Gilmore, L. A. (1999). *J. Mol. Biol.* **291**, 615–635.
Sievers, F., Wilm, A., Dineen, D., Gibson, T. J., Karplus, K., Li, W., Lopez, R., McWilliam, H., Remmert, M., Söding, J., Thompson, J. D. & Higgins, D. G. (2011). *Mol. Syst. Biol.* **7**, 539.
Tulloch, L. B., Morgan, H. P., Hannaert, V., Michels, P. A. M., Fothergill-Gilmore, L. A. & Walkinshaw, M. D. (2008). *J. Mol. Biol.* **383**, 615–626.
Valentini, G., Chiarelli, L. R., Fortin, R., Dolzan, M., Galizzi, A., Abraham, D. J., Wang, C., Bianchi, P., Zanella, A. & Mattevi, A. (2002). *J. Biol. Chem.* **277**, 23807–23814.
Verlinde, C. L. M. J., Hannaert, V., Blonski, C., Willson, M., Périé, J. J., Fothergill-Gilmore, L. A., Opperdoes, F. R., Gelb, M. H., Hol, W. G. J. & Michels, P. A. M. (2001). *Drug Resist. Updat.* **4**, 50–65.
Williams, R., Holyoak, T., McDonald, G., Gui, C. & Fenton, A. W. (2006). *Biochemistry*, **45**, 5421–5429.
Winn, M. D. *et al.* (2011). *Acta Cryst.* D**67**, 235–242.
Wooll, J. O., Friesen, R. H. E., White, M. A., Watowich, S. J., Fox, R. O., Lee, J. C. & Czerwinski, E. W. (2001). *J. Mol. Biol.* **312**, 525–540.